J. Fluid Mech. (2015), *vol.* 772, *pp.* 784–804. © Cambridge University Press 2015
doi:10.1017/jfm.2015.190

Landslide tsunamis in lakes

Louis-Alexandre Couston[1], Chiang C. Mei[2] and Mohammad-Reza Alam[1,†]

[1]Department of Mechanical Engineering, University of California, Berkeley, CA 94720, USA

[2]Department of Civil and Environmental Engineering, Massachusetts Institute of Technology, Cambridge, MA 02139, USA

(Received 2 May 2014; revised 29 October 2014; accepted 20 March 2015;
first published online 11 May 2015)

Landslides plunging into lakes and reservoirs can result in extreme wave runup at the shores. This phenomenon has claimed lives and caused damage to near-shore properties. Landslide tsunamis in lakes are different from typical earthquake tsunamis in the open ocean in that (i) the affected areas are usually within the near field of the source, (ii) the highest runup occurs within the time period of the geophysical event, and (iii) the enclosed geometry of a lake does not let the tsunami energy escape. To address the problem of transient landslide tsunami runup and to predict the resulting inundation, we utilize a nonlinear model equation in the Lagrangian frame of reference. The motivation for using such a scheme lies in the fact that the runup on an inclined boundary is directly and readily computed in the Lagrangian framework without the need to resort to approximations. In this work, we investigate the inundation patterns due to landslide tsunamis in a lake. We show by numerical computations that Airy's approximation of an irrotational theory using Lagrangian coordinates can legitimately predict runup of large amplitude. We also demonstrate that in a lake of finite size the highest runup may be magnified by constructive interference between edge waves that are trapped along the shore and multiple reflections of outgoing waves from opposite shores, and may occur somewhat after the first inundation.

Key words: coastal engineering, shallow water flows, surface gravity waves

1. Introduction

Landslide-generated large waves are often reported in lakes, bays and large reservoirs. A tragic event of this type happened in 1963 when a massive landslide behind Vajont dam in Italy resulted in large waves that overflowed the dam crest and took more than 2000 lives in the neighbouring villages (e.g. Genevois & Ghirotti 2005). The overflow of water was estimated at 30 million cubic metres. Landslide tsunamis and associated damage have been reported for numerous lakes and partially enclosed bodies of water such as Spirit Lake in Washington State (Voight *et al.* 1983), Lake Loen in Norway (Jorstad 1968; Bryant 2008), Lake Tahoe in California (Gardner, Mayer & Hughs Clarke 2000), Lituya Bay in Alsaska, with ∼500 m runup, called a Mega-Tsunami (Frits, Mohammed & Yoo 2009; Weiss, Fritz & Wünnemann 2009),

†Email address for correspondence: reza.alam@berkeley.edu

and frequently at Lake Roosevelt in Washington State (Lockridge 1990; Bryant 2008) and in the Volga river in Russia (Didenkulova & Pelinovsky 2007). Aside from taking lives and causing damage to nearshore houses and facilities, lake tsunamis make navigation hazardous by moving mud, stones and other debris such as fallen trees and destroyed houses.

Along an open coast the first few leading waves of a tsunami are usually responsible for the majority of the destruction. Tsunamis in lakes or in other enclosed water bodies are different in that: (i) the affected areas are near the source of disturbance, (ii) destructive runups may occur close to the time of the initial entry, and (iii) waves do not escape or disperse but are reflected back and forth until damped into heat and turbulence. Thus far, numerical prediction of runup on shores of complex bathymetry is still an arduous task, due to a number of difficulties such as: (i) moving shoreline, (ii) onset and propagation of breaking waves, and (iii) interaction with stationary or moving objects. To overcome all these challenges, direct numerical simulation taking full account of nonlinearity and turbulence is necessary. In practice, however, coastal planning and warning procedures require efficient forecasting schemes based on approximate models.

For tsunamis originating from distant earthquakes, numerical models based on linear theory can be quite adequate in accounting for dispersion and scattering during transoceanic propagation. Upon entering the continental shelf, wave amplitude increases and frequency dispersion diminishes. While the Boussinesq approximation is a good basis for modelling weakly nonlinear long waves before reaching the shore, coastal flooding calls for mathematical models capable of predicting highly nonlinear waves in very shallow water or on dry land.

Airy's approximation for nonlinear long waves has been used in the conventional Eulerian framework to predict the runup of moderately steep waves on beaches, with amplitudes comparable to or larger than the local water depth. On this basis, an analytical theory for the runup on an infinitely long plane beach was put forward by Carrier & Greenspan (1958). The theory is based on the hodograph transformation of the shallow-water equations, and has the advantage of including the shoreline motion in the final solution. While several interesting extensions have been investigated (e.g. Tuck & Hwang 1972; Spielvogel 1975; Tadepalli & Synolakis 1994; Kânoğlu 2004; Zahibo *et al.* 2006; Didenkulova, Kurkin & Pelinovsky 2007*b*; Madsen & Schäffer 2010; Rybkin, Pelinovsky & Didenkulova 2014), the complexity of the solution and its restriction to idealized problems have limited its use (see Pelinovsky & Mazova 1992; Carrier, Wu & Yeh 2003). To account for complex bathymetries and three-dimensional problems, numerical codes have been developed by patching computations based on Airy's or Boussinesq's approximation near the shore and linearized approximation far offshore (see for instance Yeh, Liu & Synolakis 1996).

Discrete computations based on Airy's equations in the Eulerian formulation require special care in the prediction of the moving shoreline. The challenge is that the horizontal extent of the computational domain with fixed grid points must be adjusted in time as waves run up and down. Different methods developed to predict the horizontal motion of the wet/dry interface can be found in the literature (see for instance Balzano 1998; Lynett & Liu 2002). These so-called wetting/drying algorithms are, however, approximate with specific accuracy/efficiency trade-offs, and their implementation is difficult to generalize as they typically depend on the specific model equations used (e.g. Boussinesq or Airy) as well as the particular numerical method chosen (e.g. finite volume or finite element, cf. e.g. Tchamen & Kahawita 1998; Medeiros & Hagen 2013). A convenient alternative is to work in the less-used

Lagrangian frame of reference. In the Lagrangian framework the fluid flow is obtained by following the trajectory of each fluid particle $\boldsymbol{x}(\boldsymbol{a}, t) = (x, y, z)$, which is regarded as an unknown function of the fluid particle's initial position $\boldsymbol{a} = (a, b, c)$ and the time t. The elevation and horizontal extent of the free surface are thus known at all times, as required by the kinematic condition. Therefore an immediate advantage of the Lagrangian formulation is that the free surface and the moving shoreline are known *a priori* and are defined by their initial positions.

Historically, Airy was the first to derive the nonlinear long-wave equation for a horizontal seabed using Lagrangian coordinates (Airy 1841; Lamb 1932). The solution for the runup of small-amplitude (linear) waves on a uniformly sloping beach was later obtained in the Lagrangian framework by Miche (1944), and was rederived in the limit of long waves by Shuto (1967). Interestingly this linear runup solution is identical to the analytical prediction based on the nonlinear long-wave equation in Eulerian coordinates for periodic water waves (cf. Carrier & Greenspan 1958). The Lagrangian theory for shallow-water waves was subsequently expanded by Shuto (1968, 1972), Shuto & Goto (1978), Goto (1979), Goto & Shuto (1979), Goto & Shuto (1980), Johnsgard & Pedersen (1997) and Fujima (2007) to account for nonlinearity, arbitrary seabed topography and bottom deformation in two horizontal dimensions. Weakly nonlinear and weakly dispersive equations, similar to the Boussinesq equations in Eulerian coordinates, have also been investigated in the Lagrangian framework (cf. Pedersen & Gjevik 1983; Zelt 1986; Jensen, Pedersen & Wood 2003), with applications to wave runup investigations and harbour oscillations (cf. Zelt & Raichlen 1990).

In this article we shall use the long-wave approximation of Airy in the Lagrangian framework (Johnsgard & Pedersen 1997; Fujima 2007) for the numerical prediction of two-dimensional tsunamis, created by landslides, in a shallow lake. We solve the governing equations with a fourth-order Runge–Kutta method for time integration, and a compact finite-difference scheme for spatial differentiation. For the wave generation mechanism, we consider a solid subaerial slide moving at a constant speed down a sloping beach of an enclosed basin. Physical implications of three-dimensionality on the wave pattern are discussed and quantitative improvements over the linear approximation are assessed.

2. Long-wave equations in Lagrangian coordinates

Consider wave propagation on the surface of a homogeneous, inviscid and incompressible fluid. We define a Cartesian coordinate system with x- and y-axes on the mean free surface and z-axis positive upward. Let the initial and current locations of a fluid particle be denoted respectively by (a, b, c) and (x, y, z). Then the equation for mass conservation reads

$$\frac{\partial(x, y, z)}{\partial(a, b, c)} = 1, \tag{2.1}$$

and the momentum equation requires (e.g. Lamb 1932)

$$\begin{pmatrix} x_a & y_a & z_a \\ x_b & y_b & z_b \\ x_c & y_c & z_c \end{pmatrix} \begin{Bmatrix} x_{tt} \\ y_{tt} \\ z_{tt} + g \end{Bmatrix} + \frac{1}{\rho} \begin{Bmatrix} p_a \\ p_b \\ p_c \end{Bmatrix} = 0, \tag{2.2}$$

in which, ρ is the fluid density, g the gravity acceleration, and p the pressure. Assuming that the atmospheric pressure on the free-surface ($c = 0$) is uniform, the dynamic boundary conditions become

$$x_{tt}x_a + y_{tt}y_a + (z_{tt} + g)z_a = 0, \quad c = 0, \tag{2.3a}$$

$$x_{tt}x_b + y_{tt}y_b + (z_{tt} + g)z_b = 0, \quad c = 0. \tag{2.3b}$$

Note that the free-surface height above the still water level is given by $\eta = z(a, b, 0, t)$. Assuming a time-varying water depth $h(x, y, t)$, the seabed is represented by $c = -h_0(a, b) = -h(a, b, t = 0)$. Then the kinematic boundary condition on the bottom reads

$$z(a, b, c, t) = -h(x, y, t), \quad c = -h_0(a, b). \tag{2.4}$$

As in Airy's theory in Eulerian coordinates we consider long waves in shallow water and assume that the vertical displacement of fluid particles, i.e. the wave amplitude A, is comparable to the typical water depth H, but much smaller than the horizontal length scale L, i.e.

$$\mu = \frac{H}{L} \ll 1, \quad \frac{A}{H} = O(1). \tag{2.5a,b}$$

The relevant set of approximate equations for long-wave propagation will be obtained by employing dimensionless variables, denoted by asterisks, as follows:

$$(x, y, a, b) = L(x^*, y^*, a^*, b^*), \quad (z, c, h_0, h, \eta) = H(z^*, c^*, h_0^*, h^*, \eta^*), \quad t = \frac{L}{\sqrt{gH}}t^*. \tag{2.6a–c}$$

From this point on all our equations will be in the dimensionless form and we will drop the asterisks for notational simplicity. We define the fluid displacement vector $\boldsymbol{X}(a, b, c, t) = (X, Y, Z)$ by

$$x = a + X, \quad y = b + Y, \quad z = c + Z. \tag{2.7a–c}$$

Expanding the displacement vector in a power series of the vertical coordinate, i.e.

$$\boldsymbol{X} = \sum_{n=0}^{\infty} c^n \boldsymbol{X}^{(n)}(a, b, t), \tag{2.8}$$

and invoking irrotationality,

$$\frac{\partial(x, y, y_t)}{\partial(a, b, c)} = \mu^2 \frac{\partial(x, z_t, z)}{\partial(a, b, c)}, \quad \frac{\partial(x, y, x_t)}{\partial(a, b, c)} = \mu^2 \frac{\partial(z_t, y, z)}{\partial(a, b, c)}, \quad \frac{\partial(y_t, y, z)}{\partial(a, b, c)} = \frac{\partial(x, x_t, z)}{\partial(a, b, c)}, \tag{2.9a–c}$$

it can be shown that $(X, Y) = (X^{(0)}, Y^{(0)}) + O(\mu^2)$ and $Z = Z^{(0)} + cZ^{(1)} + O(\mu^2)$. This implies, as expected for shallow-water waves, that the horizontal flow is vertically uniform, and as a result the pressure is hydrostatic. To the leading order, it is thus sufficient to solve the free-surface conditions (2.3) for the variables $X^{(0)}$ and $Y^{(0)}$ only.

Noting that (X_0, Y_0) are independent of c, after some algebra, we obtain from (2.3)

$$X_{tt}^{(0)} = \frac{Y_a^{(0)} Z_b^{(0)} - (1 + Y_b^{(0)}) Z_a^{(0)}}{1 + X_a^{(0)} + Y_b^{(0)} + X_a^{(0)} Y_b^{(0)} - X_b^{(0)} Y_a^{(0)}}, \tag{2.10a}$$

$$Y_{tt}^{(0)} = \frac{X_b^{(0)} Z_a^{(0)} - \left(1 + X_a^{(0)}\right) Z_b^{(0)}}{1 + X_a^{(0)} + Y_b^{(0)} + X_a^{(0)} Y_b^{(0)} - X_b^{(0)} Y_a^{(0)}}, \tag{2.10b}$$

where

$$Z^{(0)} = h_0(a, b) Z^{(1)} + h_0(a, b) - h(a + X^{(0)}, b + Y^{(0)}, t) \tag{2.11}$$

is the vertical displacement of the free surface as obtained from the seabed condition (2.4), with

$$Z^{(1)} = -\frac{X_a^{(0)} + Y_b^{(0)} + X_a^{(0)} Y_b^{(0)} - X_b^{(0)} Y_a^{(0)}}{1 + X_a^{(0)} + Y_b^{(0)} + X_a^{(0)} Y_b^{(0)} - X_b^{(0)} Y_a^{(0)}} \tag{2.12}$$

due to equation (2.1) for mass conservation. Equations (2.10) are dispersionless and are valid for simulation time of $t \leqslant O(1/\mu)$.

Once the solution to the Lagrangian equations (2.10) is known, the free-surface elevation is obtained from $\eta(x, y, t) = Z(a, b, c = 0, t)$. To find the free-surface elevation in the Eulerian framework, i.e. $\eta(x, y, t)$, we need to invert the nonlinear system

$$x = a + X^{(0)}(a, b, t), \quad y = b + Y^{(0)}(a, b, t), \tag{2.13a,b}$$

to get

$$a = a(x, y, t), \quad b = b(x, y, t), \quad c = 0, \tag{2.14a–c}$$

and substitute the results into (2.11). This transformation can be done as long as the Jacobian, defined by $\partial(x, y)/\partial(a, b)$, is non-zero (see Zelt 1986, for more details).

2.1. *One-dimensional limit*

For one-dimensional propagation ($Y = \partial/\partial b = 0$) the continuity equation (2.12) becomes

$$Z^{(1)} = -\frac{X_a^{(0)}}{1 + X_a^{(0)}}. \tag{2.15}$$

With the help of (2.11), the free-surface condition (2.10*a*) is then simplified to

$$X_{tt}^{(0)} \left(1 + X_a^{(0)}\right) + \left[h_0(a) - h(a + X^{(0)}, t)\right]_a - \left[\frac{h_0(a) X_a^{(0)}}{1 + X_a^{(0)}}\right]_a = 0. \tag{2.16}$$

This equation will be solved numerically for model validation in § 3.2. Note that in the constant water-depth case, i.e. $h = h_0 = 1$, (2.16) further reduces to

$$X_{tt}^{(0)} = \frac{X_{aa}^{(0)}}{\left(1 + X_a^{(0)}\right)^3}, \tag{2.17}$$

which was first given by Airy and is similar to the equation that governs the oscillations of nonlinear strings (Zabusky 1962).

2.2. *Linearized limit*

Assuming that $\boldsymbol{X} \sim O(\epsilon) \ll 1$ the linearized form of (2.12), (2.10*a*) and (2.10*b*) is obtained as

$$Z^{(1)} = -X_a^{(0)} - Y_b^{(0)}, \tag{2.18a}$$

$$X_{tt}^{(0)} = -Z_a^{(0)}, \tag{2.18b}$$

$$Y_{tt}^{(0)} = -Z_b^{(0)}. \tag{2.18c}$$

Let us now consider that the seafloor deforms over time because of the passage of a landslide. Assuming this perturbation to be small we can rewrite the water depth as $h(x, y, t) = h_0(x, y) + f(x, y, t)$ where $f \sim O(\epsilon)$. In this case, by Taylor expanding h and substituting (2.18*a*) in (2.11), the leading-order free-surface height is obtained as

$$\eta(x, y, t) = -f(x, y, t) - \boldsymbol{\nabla}_h \cdot \left\{ h_0 \begin{bmatrix} X^{(0)} \\ Y^{(0)} \end{bmatrix} \right\} \tag{2.19}$$

where $\boldsymbol{\nabla}_h = (\partial/\partial a, \partial/\partial b)$. Taking the second time-derivative of (2.19), and using (2.18*b*), (2.18*c*) we obtain

$$\begin{aligned} \eta_{tt} + f_{tt} &= -h_0 \left(X_{a,tt}^{(0)} + Y_{b,tt}^{(0)} \right) - h_{0,a} X_{tt}^{(0)} - h_{0,b} Y_{tt}^{(0)} \\ &= h_0 \left(Z_{aa}^{(0)} + Z_{bb}^{(0)} \right) + h_{0,a} Z_a^{(0)} + h_{0,b} Z_b^{(0)} \\ &= [h_0 Z_a^{(0)}]_a + [h_0 Z_b^{(0)}]_b. \end{aligned} \tag{2.20}$$

Since $\eta = Z^{(0)}$, $X = x - a \sim O(\epsilon)$ and $Y = y - b \sim O(\epsilon)$, the above equation readily reduces to the classical shallow-water equation in the Eulerian frame of reference

$$\eta_{tt} + f_{tt} = [h_0(x, y)\eta_x]_x + [h_0(x, y)\eta_y]_y. \tag{2.21}$$

Equation (2.21), first derived by Tuck & Hwang (1972), has an analytical closed-form solution in one- and two-dimensional setups (Liu, Lynett & Synolakis 2003; Sammarco & Renzi 2008; Didenkulova & Pelinovsky 2013).

2.3. *Wave energy in a Lagrangian framework*

To derive the expression for wave energy in terms of Lagrangian variables we first consider the Eulerian definition of wave energy (normalized by $\rho g H^2 L^2$) in the domain $\Omega = \{(x, y, z) \in \mathscr{F}(t) \times [-h(x, y, t), \eta(x, y, t)]\}$ where $\mathscr{F}(t) \subset \mathbb{R}^2$ is the horizontal projection of the free surface (that extends from one side's runup or rundown to the other side's runup or rundown):

$$\mathscr{E} = \mathscr{E}_{pot} + \mathscr{E}_{kin} = \int_{\mathscr{F}(t)} \int_0^{\eta} z \, \mathrm{d}z \, \mathrm{d}x \, \mathrm{d}y + \int_{\mathscr{F}(t)} \int_{-h}^{\eta} \frac{1}{2} (x_t^2 + y_t^2 + \mu^2 z_t^2) \, \mathrm{d}z \, \mathrm{d}x \, \mathrm{d}y. \tag{2.22}$$

Since $\mu = H/L \ll 1$, we see from (2.22) that the contribution of the vertical velocity is negligible. The potential energy $\mathscr{E}_{pot}$ readily reduces to

$$\int_{\mathscr{F}(t)} \frac{1}{2} \eta^2 \, \mathrm{d}x \, \mathrm{d}y. \tag{2.23}$$

Changing the variables of integration (x, y, z) to the Lagrangian coordinates (a, b, c) and noting that $\eta(x, y, t) = Z(a, b, 0, t)$, $\boldsymbol{x}_t = \boldsymbol{X}_t$, we rewrite the total wave energy as

$$\mathscr{E} = \frac{1}{2}\int_{\mathscr{F}(0)} \left[\left.\frac{\partial(x, y)}{\partial(a, b)}\right|_{c=0} Z^2(a, b, 0, t) + \int_{-h_0(a,b)}^{0} \frac{\partial(x, y, z)}{\partial(a, b, c)} \left(X_t^2 + Y_t^2 + \mu^2 Z_t^2\right) \mathrm{d}c \right] \mathrm{d}a\, \mathrm{d}b, \tag{2.24}$$

where clearly the determinant $\partial(x, y, z)/\partial(a, b, c) = 1$ because of continuity. Note that $\mathscr{F}(0)$ is the projection of the initial (flat) water surface and therefore gives the limits of integration for the Lagrangian variables a, b in (2.24). Also it is to be noted that the vertical limit of integration is from $-h_0(a, b)$ to 0, again because the integration is performed over Lagrangian variables. The final form of total wave energy is obtained once Airy's expansion is substituted for the displacement variables. To the leading order, we get

$$\mathscr{E} = \frac{1}{2}\int_{\mathscr{F}(0)} \left[\frac{\partial(a + X^{(0)}, b + Y^{(0)})}{\partial(a, b)} (Z^{(0)})^2 + h_0 \left((X_t^{(0)})^2 + (Y_t^{(0)})^2 \right) \right] \mathrm{d}a\, \mathrm{d}b. \tag{2.25}$$

3. Numerical implementation

3.1. *Finite-difference scheme*

We solve the system of equations (2.10) by the finite-difference method. Equations (2.10) are integrated in time using an explicit fourth-order method (Runge–Kutta 4) with $Z^{(0)}$ obtained from (2.11) and (2.12). A compact finite-difference Padé scheme is implemented to obtain the first- and second-order spatial derivatives such that the accuracy of the numerical scheme is that of a fourth-order method. The computation of the derivatives on the edges of the domain depends on the type of the boundary. For a vertical wall, which acts as a mirror, the normal displacement is zero, and the tangential displacement has a vanishing normal derivative. For a shoreline, which we define as the intersection of a sloping beach with the free surface, a forward or backward approximation is used in space to get the horizontal derivatives. The discretization of the derivatives on the boundaries is performed by adjusting the number of stencil points so that the order of approximation is the same as in the interior of the domain.

We shall assume perfect reflection at the shore and require the solution to be bounded everywhere including near the moving shoreline. Since for the linearized problem on a plane beach one of the homogeneous solutions is proportional to the Weber function Y_0 in two dimensions (Bessel functions of the second kind) and to the Whittaker function $W_{n^2/2m,0}$ in three dimensions ($n, m \in \mathbb{N}$), which are both unbounded at the origin (see e.g. Shuto 1967, 1968), small errors in numerical approximations can induce instability. Indeed for the two-dimensional problem one obtains Bessel's equation for a plane sloping beach, i.e. by substituting $h(a) = a\tan\alpha$ in (2.16), which presents a singularity at the shoreline $a = 0$. To resolve this issue numerically, we integrate the governing equations up to one grid cell before the shoreline. As a result, the physical shoreline is not part of the numerical domain, and is determined by a linear extrapolation from the grid boundary. The grid size is chosen small enough such that convergence is secured.

3.2. *Model validation*

Numerical predictions of wave runup on a sloping beach based on our model equations are compared with analytical solutions of the celebrated hodograph-transformed shallow-water equations of Carrier & Greenspan (1958). Specifically,

Case		Max. runup	Min. rundown	Max. shoreward speed	Max. seaward speed
a′	(i)	0.02343	−0.01352	−0.05043 at $x=-0.0142$	0.1087 at $x=0.000856$
	(ii)	(0.0235)	(−0.0134)	(−0.0514 at $x=-0.0142$)	(0.1066 at $x=0.000376$)
a	(i)	0.0467	−0.0272	−0.0991 at $x=-0.0258$	0.222 at $x=0.0153$
	(ii)	(0.0470)	(−0.0268)	(−0.103 at $x=-0.0260$)	(0.213 at $x=0.0122$)

TABLE 1. Comparison of wave runup extrema on an idealized beach ($h(x)=x$) between: (i) numerical simulations of (2.16) and (ii) the analytical solution derived by Carrier *et al.* (2003) (in parentheses). The initial Gaussian waveform is described by (3.1) with amplitude $H_1=0.017/2$ for case **a′** and $H_1=0.017$ for case **a**. Other parameters are $c_1=4.0$, $x_1=1.69$. The analytical results for case **a** are the ones reported in Carrier *et al.* (2003) (with sign of the runup/rundown changed to correspond to runup heights instead of penetration depths), while those of case **a′** are based on a numerical integration of (2.9) in Kânoğlu (2004). The numerical simulations results are given for $\delta a=2\times10^{-3}$, $\delta t=4.88\times10^{-5}$.

we consider an initial Gaussian waveform with zero velocity, i.e. case **a** in Carrier *et al.* (2003), which in the Eulerian framework reads

$$\eta(x,0)=H_1\exp(-c_1(x-x_1)^2),\quad \text{with } \eta_t(x,0)=0. \tag{3.1}$$

Since case **a** of Carrier *et al.* (2003) (i.e. with $H_1=0.017$, $c_1=4.0$, $x_1=1.69$) shows large steepnesses at the shoreline tip, which is not permitted under Airy assumptions, here we first compare our numerical predictions with the analytical solution obtained for an initial Gaussian waveform with a reduced amplitude of $H_1=0.017/2$ but with c_1, x_1 as before. Extreme values such as maximum runup and rundown are compared in table 1 for this case, referred to as **a′**, and a very good agreement is obtained. Although large wave steepnesses at the shoreline invalidates our model assumptions (see the discussion of Meyer 1986*a*,*b*, on this), we still compare our numerical predictions with the analytical solution for the original case **a** of Carrier *et al.* (2003). The Jacobian of the hodograph transformation has been shown to change sign very close to the shoreline in this case (cf. figure 17 in Carrier *et al.* 2003), which is an indicator of wave breaking. It was, however, remarked by Synolakis (1987), who conducted laboratory experiments on solitary waves, that the post-breaking analytical wave profile approximates the actual wave very well when wave breaking occurs very close to the shoreline. The fact that we obtain a very good match in table 1 for the original case **a** of Carrier *et al.* (2003) suggests that numerical simulations may continue to predict accurate wave shape despite having waves breaking at the shoreline. This is of course permitted by the fact that we moved the first grid point away from the line of vanishing depth. We would like to point out that in our direct simulation of the governing equation (2.16) for case **a** the wave steepness, which is given by

$$\eta_x=\left[\frac{z_a(a,c,t)}{x_a(a,c,t)}\right]_{c=0}=\left[\frac{Z_a(a,c,t)}{1+X_a(a,c,t)}\right]_{c=0}, \tag{3.2}$$

grows unbounded as we decrease the grid size (figure 1*a*), i.e. wave steepness at the shoreline does not converge. This is not unexpected since the Jacobian of the hodograph transformation in this case vanishes at the shoreline as discussed before. The runup itself, however, converges to the true runup value. For case **a′**,

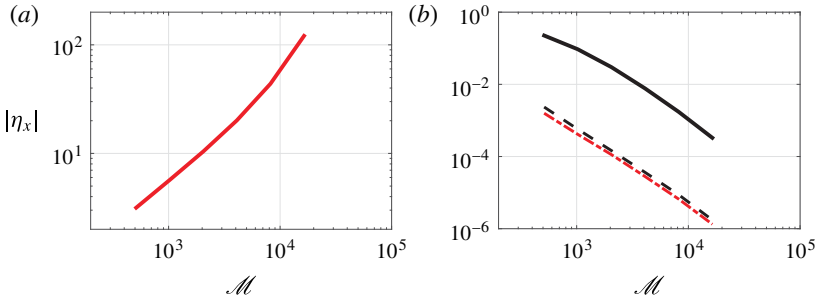

FIGURE 1. (Colour online) (*a*) Absolute value of the maximum wave steepness at the shoreline as a function of the number of grid points $\mathscr{M}$ for case **a** reported in table 1. Clearly in this case $|\eta_x|$ grows exponentially with $\mathscr{M}$ and does not converge. (*b*) The relative error of the maximum wave runup e_R (dashed line), and the relative error of the maximum wave steepness e_{η_x} (solid line) at the shoreline are shown as functions of $\mathscr{M}$ for the numerical simulation of case **a**′ reported in table 1. These relative errors are defined with respect to the values obtained for $\mathscr{M} = 2^{15}$ (i.e. the finest grid simulated). The relative error of the maximum wave runup for case **a** (— · —) is also shown in this plot.

i.e. with decreased wave amplitude, the Jacobian does not vanish. Correspondingly, in our simulations, both the maximum runup value and wave steepness converge asymptotically (cf. figure 1*b*).

In the following section (§ 4) we study the evolution of landslide tsunamis in a lake, and present examples that highlight the effect of nonlinearities and wave reflections and interactions in the inundation maps that are specific to lakes and enclosed bodies of water.

4. Landslide tsunamis in lakes

4.1. *The setup*

Let us focus our attention on a geometrically simple lake to highlight some of the physics involved. Specifically, we consider a shallow lake of rectangular surface area $L_a \times 2L_b$ confined symmetrically by two opposing vertical walls along $y = \pm L_b$ and two opposing sloping beaches aligned with the $\pm x$ direction (figure 2). A vertical wall may be an idealization of a mountain cliff or a dam. We assume that the two opposing beaches have the same slopes, and that they each occupy 1/3 of the horizontal extent of the lake. The remaining middle 1/3 is flat with the dimensionless depth of unity; therefore the beach slope is $\tan\alpha = 3/L_a$ in the dimensionless space and $\mu \tan\alpha$ in the physical domain (note that in the dimensionless space vertical and horizontal lengths are scaled differently, cf. (2.6*a*, *b*)). The bottom is therefore given by

$$h_0(x, y) = \begin{cases} x\tan\alpha, & 0 < x < L_a/3, \quad -L_b < y < L_b, \\ 1, & L_a/3 < x < 2L_a/3, \quad -L_b < y < L_b, \\ 3 - x\tan\alpha, & 2L_a/3 < x < L_a, \quad -L_b < y < L_b. \end{cases} \tag{4.1}$$

To avoid sharp corners an arc of radius 1/20 (in dimensionless variables) connects each sloping beach to the flat bottom.

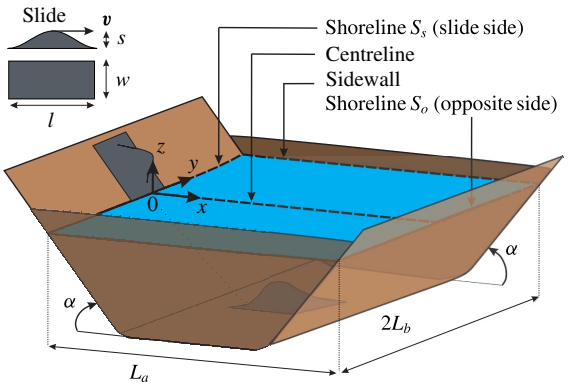

FIGURE 2. (Colour online) Schematic of the lake and the landslide. The landslide is shown at both its initial position (above water) and its final position (underwater).

We consider the motion of a landslide whose height is given by

$$h_s(x, y, t) = \begin{cases} -s \sin^2\left[\frac{\pi}{l}(x - vt)\right] \cos^2\left(\frac{\pi}{w}y\right), & \text{for } -l < x - vt < 0, \ -\frac{w}{2} < y < \frac{w}{2}, \\ 0, & \text{otherwise,} \end{cases} \tag{4.2}$$

which describes a smooth and rigid hump-like landslide with a horizontally projected surface area of length l, width w and maximum thickness s that moves along the lake centreline (figure 2). The total water depth is therefore $h(x, y, t) = h_0(x, y) + h_s(x, y, t)$. Physically speaking, (4.2) corresponds to a slide moving with a constant speed $v\sqrt{1 + \tan^2\alpha}$ down the beach. When the centre of the slide reaches the beach toe at $x = L_a/3$, it decelerates according to a smooth cubic law $v \propto t^3$ until it reaches the middle of the lake where it stops (i.e. at $x = L_a/2$, cf. figure 2).

Two types of waves are generated by the three-dimensional subaerial landslide as it enters the water. We refer to waves that propagate freely across the lake as *outgoing waves*, and to waves that are trapped by the shoreline as *edge waves*. Outgoing waves along open coasts, forced impulsively by landslides, have been the subject of a large number of laboratory experiments conducted for both solid landslides (e.g. Kamphuis & Bowering 1970; Walder 2003; Panizzo, De Girolamo & Petaccia 2005*a*; Panizzo *et al.* 2005*b*; Heller *et al.* 2012) and granular landslides (Fritz, Hager & Minor 2004; Ataie-Ashtiani & Nik-Khah 2008; Di Risio, De Girolamo & Beltrami 2011). More recently, properties of landslide-generated edge waves have also been investigated (e.g. Liu *et al.* 2005; Lynett & Liu 2005; Sammarco & Renzi 2008; Di Risio *et al.* 2009). The following analysis of landslide tsunamis in lakes highlights the importance of nonlinearity as well as the significance of the interactions between outgoing and edge waves in the generation of unexpectedly large runups.

4.2. *Numerical results and discussion*

We choose the lake dimensions $L_a = 1$, $L_b = 1.02$ and normalized slopes of $\tan\alpha = 3$. A solid mass of $w = l = 0.25$ with thickness $s = 0.07$ according to (4.2) slides down the beach S_s with a horizontal speed $v = 0.12$ (this specific set of parameters is chosen as it further highlights the physics to be discussed). A detailed sensitivity analysis is

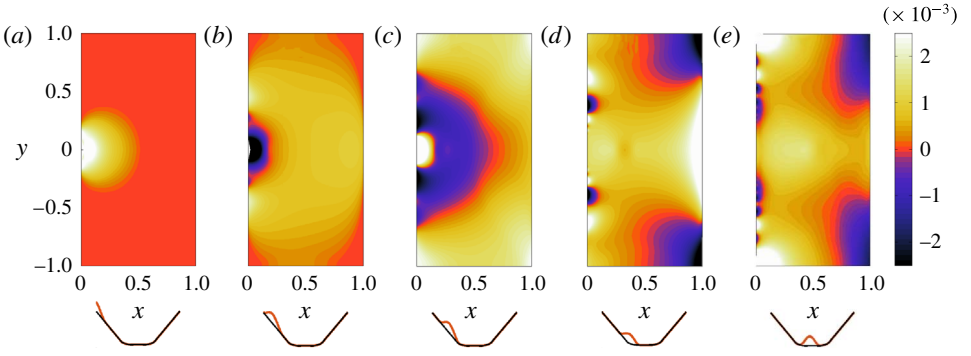

FIGURE 3. (Colour online) Snapshots of nonlinear dimensionless free-surface height Z at (*a*) $t = 0.83$, (*b*) $t = 1.66$, (*c*) $t = 2.47$, (*d*) $t = 3.76$, (*e*) $t = 5.63$. Physical parameters associated with the lake dimensions and slide shape are $s = 0.07$, $v = 0.12$, $L_b = 1.02$, $w = l = 0.25$, $\tan\alpha = 3$. Simulation parameters are $\delta a = 0.002$, $\delta b = 0.002$, $\delta t = 0.001$. The position of the slide with respect to the lake geometry is shown below each plot (slide height is magnified by a factor of four).

provided later. Simulation parameters are chosen to be $\delta a = 0.002$, $\delta b = 0.002$, with Courant number equal to 0.5 such that $\delta t = 0.001$, for which our simulations converge.

Snapshots of the water surface are shown in figure 3(*a–e*). Lighter colours show higher elevations and darker colours show depressions. Upon water entry at $t = 0$ the land mass pushes the water forward, generating a big hump of water at its front (figure 3*a*). This first hump then disintegrates into a radially spreading outgoing wave and a series of shoreline-trapped edge waves on the slide side S_s. A pair of edge-wave crests can be seen in figure 3(*b*) travelling away from the centreline $y = 0$. The outgoing wave crosses the length of the lake and reaches the opposite shoreline S_o (figure 3*b*), while a ring of depression is formed near the origin on the S_s shore. Moments later (figure 3*c*), the first outgoing and edge waves reach the corners of the lake ($y = \pm L_b$) while a second hump is formed at the origin. Figure 3(*d*) shows the runup of the second outgoing wave on S_o, and the propagation of the edge waves resulting from the disintegration of the rebound hump along S_s. The leading edge wave of this second hump is the longest and largest in amplitude, as seen in white at $y \sim 0.63$ in figure 3(*d*). Finally, figure 3(*e*) shows the return of the second outgoing wave (the one initiated on S_s in figure 3*c*) to S_s after reflection from S_o. This reflected wave superimposes on the trail of edge waves on S_s, resulting in higher runups at some locations along S_s, as will be elaborated shortly.

The time history of the water surface evolution along the shoreline S_s ($x = 0$) is shown in figure 4(*a*), the shoreline S_o ($x = L_a$) in 4(*b*), the centreline of the lake ($y = 0$) in 4(*c*), and the vertical sidewalls ($y = \pm L_b$) in 4(*d*). The first runup due to the water entry of the landslide is seen in figure 4(*a*) at $y = 0$, $t \sim 0.5$. It is then followed by a rundown that starts at $t \sim 1.4$. From figure 4(*a*) it is seen that the dispersion of edge waves along S_s is similar to that resulting from an initial hump in open water: longer waves travel faster and more crests are generated as time goes by (cf. Sammarco & Renzi 2008). Due to dispersion, edge waves elongate and accelerate as they travel away from the origin (cf. Sammarco & Renzi 2008; Mei, Stiassnie & Yue 2005), as can be seen from the convex shape of the edge-wave pathlines in figure 4(*a*) (marked by solid and dashed lines).

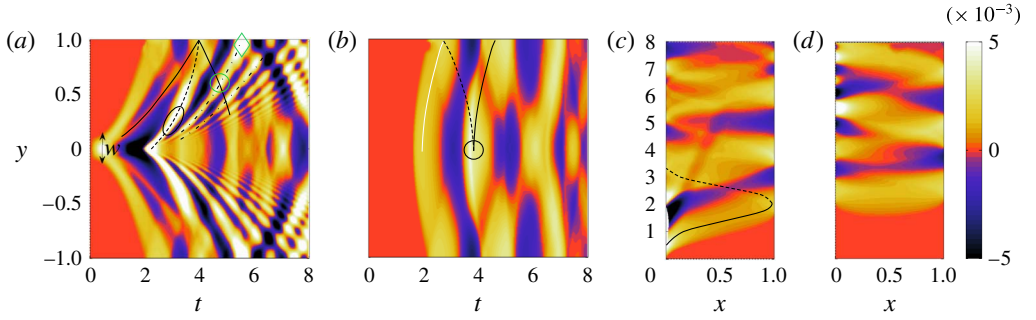

FIGURE 4. (Colour online) Time history of the nonlinear wave runup on (*a*) shoreline S_s, (*b*) shoreline S_o, and wave height along (*c*) centreline, (*d*) sidewall, for a landslide tsunami with physical and simulation parameters given in figure 3. The colour map shows the dimensionless free-surface height Z.

Figure 4(*a*) also shows the reflection of edge waves by the vertical sidewalls (i.e. $y = \pm L_b$). The second edge wave due to the first runup (solid line) meets the leading edge wave due to the second runup (dashed line) when reaching the sidewall at $y = L_b$, $t \sim 4.1$. It then bounces back to interact with the other forward moving (i.e. $+y$ direction) edge waves of the second hump (marked by dash-dotted lines). A relatively high runup at $y \sim 0.61$, $t \sim 4.8$ (highlighted by a circle) is partially due to this encounter.

The radially outgoing wave first reaches the opposite shoreline S_o at $y = 0$, $t \sim 1.7$ (figure 4*b*). Wave runup patterns along S_o (solid white and black lines) are arc-shaped due to radial spreading. The leading crest (marked by the white line) is reflected from the sidewall $y = L_b$ near S_o at $t \sim 2.7$ and turns into an edge wave whose path is marked by a black dashed line. This edge wave advances toward the centre, and interacts with the second runup (marked by a black solid line) at $t \sim 3.7$, resulting in a constructive interference (as marked by a circle). These interactions continue along S_o as more edge/outgoing waves come into play. Contrary to edge waves, outgoing waves are non-dispersive. Therefore, as seen in figure 4(*c*), the depression and elevation rays appear straight where the water depth is constant (i.e. $1/3 \leqslant x \leqslant 2/3$), and curved near the shorelines because of refraction. The superposition of the leading edge wave of the rebound (second) runup on S_s with the reflected first outgoing wave (marked by a dashed line in figure 4*c*), can be clearly seen in figure 4(*a*). The bright white spot resulting from this interaction is highlighted by an ellipse at $t \sim 3.3$. Figure 4(*c*) shows that the two outgoing crests (from the first and the second runups) remain separated for the rest of the simulations, and that the amplitude of the first outgoing wave is smaller than the second one. Figure 4(*d*) shows the surface elevation along the vertical sidewalls. Both edge waves and outgoing waves emanating from the first runup reach the sidewalls at approximately $t \sim 2.7$. They generate an almost horizontal beam across each of the two vertical walls. Edge waves on S_s ($x = 0$) are also seen in figure 4(*d*) with their crests at $t \sim 4$, 5.5, 7.5, and on S_o ($x = L_a$) at $t \sim 4.5$, 6.5.

The multiple interactions between reflected outgoing waves and edge waves that occur in a lake suggest that extreme inundations may take place far away from the immediate neighbourhood of the landslide and some time after its submergence. As an example, in our simulation, an extremely large runup occurs at the lake corners ($x = 0$, $y = \pm L_b$) due to constructive interference between the third edge wave of the initial runup, the second edge wave of the rebound (second) runup, and the reflected

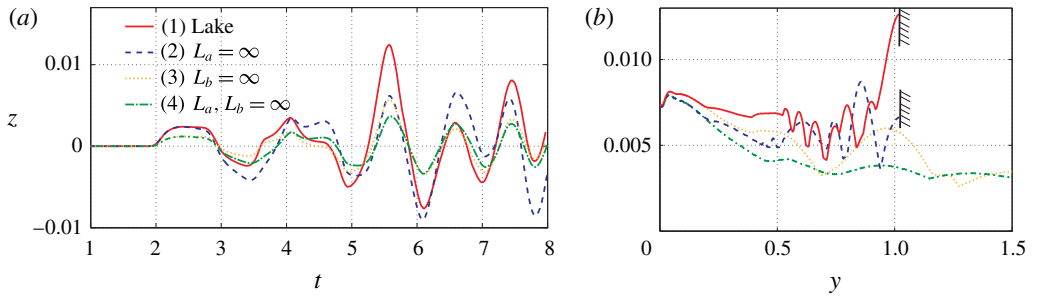

FIGURE 5. (Colour online) (*a*) Time history of nonlinear wave runup height at $y = 1.02$ on S_s for a slide entering: (1) a finite rectangular lake ($L_a = 1$, $L_b = 1.02$), (2) a long and narrow lake ($L_a = \infty$, $L_b = 1.02$), (3) a short and wide lake ($L_a = 1$, $L_b = \infty$), (4) an open coast ($L_a = \infty$, $L_b = \infty$). (*b*) Inundation maps up to $t = 8$ along S_s for $y \geqslant 0$ for the four cases displayed in (*a*). Physical and simulation parameters other than L_a and L_b are the same as in figure 3.

second outgoing wave. This runup takes place at $t = 5.5$ and is almost twice as big as any other runup along S_s (seen as a bright-coloured region in figure 4(*a*) marked by a diamond). This runup is also much larger than that estimated by an open-coast calculation, as can be seen in figure 5(*a*) where we show the wave runup at $x = 0, y = 1.02$ as a function of time due to the same slide entering four different geometric configurations: (1) a lake of finite size ($L_a = 1, L_b = 1.02$, solid line), (2) an infinitely long lake ($L_a \to \infty$, dashed line), (3) an infinitely wide lake ($L_b \to \infty$, dotted line), and (4) an open coast ($L_a, L_b \to \infty$, dash-dotted line). As expected, the runup is greatest for the finite-sized lake due to the presence of a wall at $y = L_b = 1.02$ and an opposite beach at $x = L_a = 1$. The maximum runup for the case of an infinitely long lake, infinitely wide lake and an open coast is respectively 48 %, 54 % and 71 % lower than that of the finite size lake considered here.

The inundation map of shore S_s ($y \geqslant 0$) for the four geometries considered above shows (figure 5*b*) that the average runup increases in the presence of a wall and an opposite beach. For the open coast (dash-dotted line), edge waves result in a large runup less than a quarter of the slide width away from the centreline, i.e. very close to the origin. Edge waves amplitude then decreases as they propagate farther away (which is in qualitative agreements with earlier studies by Lynett & Liu 2005; Sammarco & Renzi 2008; Di Risio *et al.* 2009). The contrast between the four cases studied here shows the importance of wave reflection from side/opposite boundaries and superposition in the magnitude and location of the maximum runup.

Of practical interest is also the importance of nonlinearities in the simulation presented. The inundation maps of the two shorelines S_s and S_o, as well as the maps of maximum wave height along the lake centreline and sidewalls, can be used to measure the significance of nonlinearity in the runup predictions. Figure 6(*a*) compares the linear versus nonlinear runup on both S_s and S_o. The maximum inundation predicted by the nonlinear theory is higher than the linear prediction everywhere on both S_s and S_o. In particular, the relative increase due to nonlinear effects at $y \sim 0.05$ on S_s is $\sim$50 %. Details of inundation curves can be better understood in the light of figure 4. For instance, the six local maxima between $y = 0.55$ and $y = 0.9$ on S_s shown in figure 6(*a*) are partially due to the reflections by the sidewall at $y = L_b$ of the third and fourth edge waves of the rebound runup interacting with trailing edge

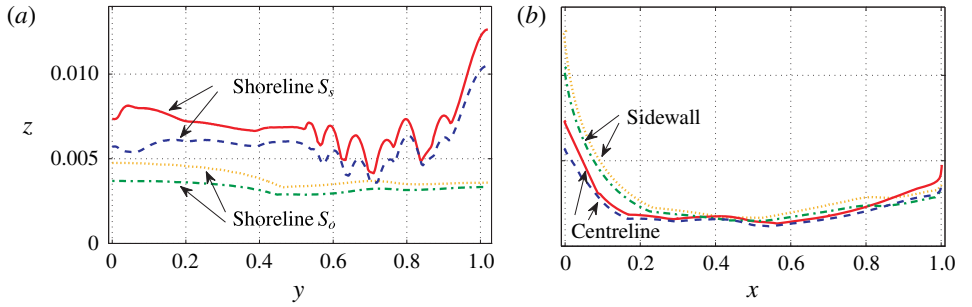

FIGURE 6. (Colour online) Inundation maps of the (*a*) shorelines S_s, S_o (for $y \geqslant 0$), and (*b*) sidewalls and centreline as predicted by nonlinear (——, · · · · · ·) and linear theories (– – –, — · —). Physical and simulation parameters are the same as in figure 3. Simulation are performed from $t = 0$ to $t = 8$ beyond which no further significant changes occur.

waves at $t \sim 7$. The extreme corner runup is found to be 20 % higher with nonlinear effects taken into account.

On the opposite shore S_o, the runup of the second outgoing wave is responsible for most of the inundation for $y < 0.5$ and is about 30 % higher when nonlinear terms are taken into account. The effects of wave shoaling and radial spreading are clearly seen in figure 6(*b*) by the rapid decrease of maximum wave height along the centreline away from the shorelines. Clearly, the quantitative difference between linear and nonlinear inundations is maximum closer to the shoreline since, due to nonlinear effects, larger wave height and steepnesses both contribute to a larger runup (cf. Didenkulova *et al.* 2007*a*).

To investigate at what time stage during the landslide event major nonlinear effects come into play and where they are highlighted, we compare the maximum linear and nonlinear wave heights for all surface fluid particles (i.e. all pairs (a, b)) at five different times (figure 7*a–e*). To quantify this difference between nonlinear and linear predictions we define

$$\mathcal{N}(a, b, t) = \frac{Z_{NL}(a, b, t) - Z_L(a, b, t)}{Z_{L,max}} \times 100, \tag{4.3}$$

where Z_{NL} (Z_L) is the maximum nonlinear (linear) wave height for each pair (a, b) and time t, and $Z_{L,max} = \max\left[Z_L(t = t_f \to \infty)\right]$ is a single number that shows the overall maximum wave height as predicted by the linear theory. In our simulations the final time $t_f = 8$ is chosen as $Z_{L,max}$ no longer changes for $t > t_f$. Stronger differences (in %) are shown with darker colours. Note that the linear results are based on (2.20).

Nonlinearity comes, as is expected, from wave–bottom interactions near the line of vanishing depth (i.e. near the shoreline). Yet the first runup on S_s, which is due to the slide starting to push the water, is only weakly nonlinear (as seen in figure 7*a*). Therefore, major nonlinearities come into play when the rebound hump is formed and disintegrates into edge waves and outgoing waves (see dark patch localized near S_s in figure 7*b*). Physically speaking, this is due to the rundown being amplified by a downward dragging imposed by the landslide descending further under the water. Excess of wave height predicted by nonlinear terms is then seen almost everywhere in the lake as edge waves and outgoing waves reach the opposite shoreline and sidewalls (figure 7*c*,*d*). Finally, figure 7(*e*) shows the contrast between maxima of nonlinear and

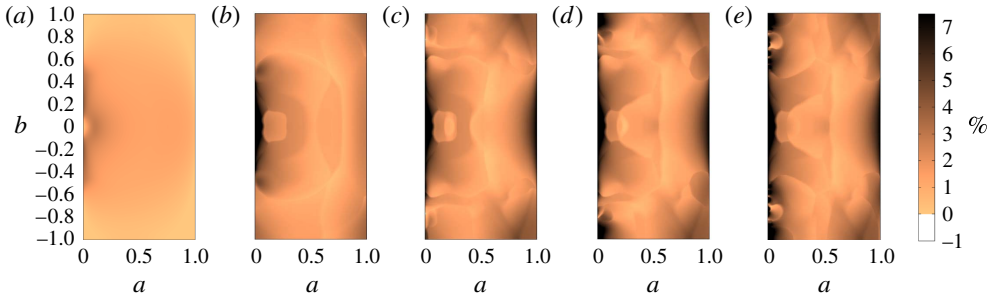

FIGURE 7. (Colour online) Spatial distribution of the difference between nonlinear and linear maximum wave heights ($\mathcal{N}$, cf. (4.3)) during a landslide tsunami in a lake. (*a–e*) show the difference during time periods lasting from zero to $t_f = 1.64$ (*a*), 3.30 (*b*), 4.97 (*c*), 6.63 (*d*), 8.00 (*e*). During the entire event, nonlinear wave-height predictions are higher than the linear ones, and the difference is higher close to the shorelines (cf. figure 6). Physical and simulation parameters are the same as in figure 3.

linear predictions from $t = 0$ to the final time $t_f = 8$. As discussed before, nonlinearity is much stronger near the shorelines and at the corners of the lake.

We remark that the strong contrast between nonlinear and linear predictions is partly due to the three-dimensional nature of the landslide-generated waves. To demonstrate this, we compare in figure 8 nonlinear and linear maximum wave heights along the lake centreline (i.e. $\mathcal{N}(a, 0, t)$) for the finite-width slide (i.e. $w < L_b$; solid line) of the case studied in figures 3–7, and an infinitely wide landslide (i.e. $w \to \infty$; dashed line), which makes the waves two-dimensional. As discussed before, the large nonlinearity $\mathcal{N}$ near $a = 0$ for the three-dimensional case in figure 8(*b*) appears with the second runup ($\mathcal{N}(a, 0, 1.6) = 16\,\%$). The much smaller difference in the two-dimensional case ($\mathcal{N}(a, 0, 1.6) = 5\,\%$) thus suggests that this increase is due to three-dimensional effects. Note that $\mathcal{N}$ is even larger than 16 % in the three-dimensional case just slightly away from the centreline ($\mathcal{N}(a, 0.05, 1.6) = 28\,\%$, cf. figure 6). Another interesting behaviour specific to the two-dimensional case is that the linear theory overpredicts the maximum wave height sometime after the slide submergence (figure 8*d*,*e* near the opposite shoreline). Note that the absolute value of $Z_{L,max}$ in the two-dimensional case can be much larger (about four times in the presented case) than its three-dimensional counterpart which is due to energy spreading in the three-dimensional case.

It is of interest also to assess how the energy ceded by the slide to the fluid is divided between edge waves and outgoing waves. For this purpose, in figure 9 we plot the total energy in the lake (solid line), the total energy very close to the shoreline S_s in the area $0 \leqslant a \leqslant 1/10$ (dash-dotted lines), and the total energy in the rest of the lake, i.e. in the area $1/10 \leqslant a \leqslant 1$ (dashed line). The total energy is calculated via (2.25) and normalized by the total wave energy in the steady state when $t \to \infty$ (here $t = 8$). The plot in figure 9(*a*) is with the same parameters as in figure 3. For comparison, we also show the spatial energy division for a smaller slide $s = 0.07/2$ that moves: (i) at the original speed $v = 0.12$ (figure 9*b*), and (ii) twice as fast (i.e. $v = 0.24$, figure 9*c*). In all three cases (the first two being qualitatively very much alike) there is an overshoot of the total energy. This is because the initial outgoing wave has time to reflect on S_o back to S_s while the slide is still moving forward and opposes the motion of the reflected wave. The total energy reaches its steady-state value when the

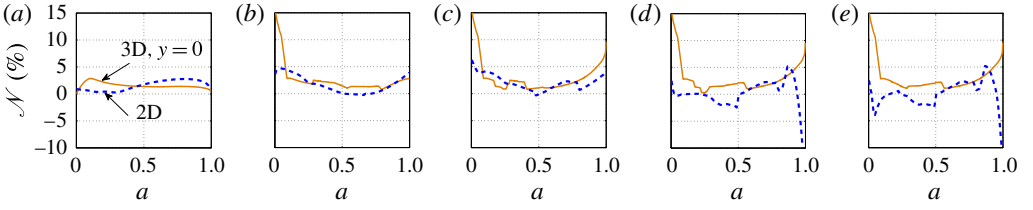

FIGURE 8. (Colour online) Effect of the slide width on the difference between nonlinear and linear maximum wave heights along the lake centreline. The predictions are plotted for a finite width landslide ($w < L_b$, ——) and an infinitely wide landslide ($w \to \infty$, – – –). In the latter case the problem is two-dimensional, and therefore this figure also highlights effects of three-dimensionality on the significance of nonlinearity. (*a*)–(*e*) The difference ($\mathscr{N}$, cf. (4.3)) for time periods from zero to $t_f = 1.64$, 3.30, 4.97, 6.63, 8.00 (i.e. same as in figure 7), respectively. Note that $\mathscr{N}$ is much higher for the three-dimensional case, and that $\mathscr{N}$ becomes negative at some time in the two-dimensional case. Physical parameters (other than w) and simulation parameters are the same as in figure 3.

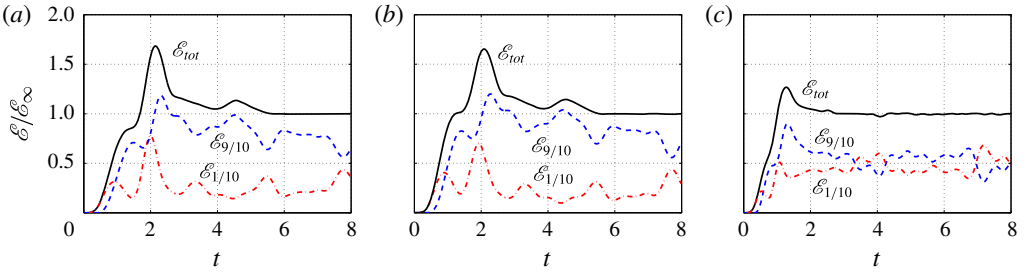

FIGURE 9. (Colour online) Wave energy in the lake ($\mathscr{E}$, cf. (2.25)) normalized by steady-state wave energy ($\mathscr{E}_\infty$) is shown for a landslide with: (*a*) $s = 0.07$, $v = 0.12$ ($\mathscr{E}_\infty = 0.967 \times 10^{-6}$); (*b*) $s = 0.035$, $v = 0.12$ ($\mathscr{E}_\infty = 0.229 \times 10^{-6}$); (*c*) $s = 0.035$, $v = 0.24$ ($\mathscr{E}_\infty = 2.220 \times 10^{-6}$). The total wave energy in the lake (——) is divided to energy in the near-S_s area ($0 < a < L_a/10$, — · —); and the rest of the lake ($L_a/10 < a < L_a$, – – –). Other physical and simulation parameters are given in figure 3.

slide stops moving, i.e. at $t = 6$ for the two slow slide cases and $t = 3$ for the faster slide.

Comparison of figures 9(*a*,*b*) and 9(*b*,*c*) shows that the slide thickness does not have a major effect on the energy distribution while slide velocity does. For the slow landslide (figure 9*a*,*b*) more energy is given to the outgoing waves and less energy is trapped, while for the fast slide the energy partitioning is almost even (figure 9*c*). In figure 9(*b*), the first two humps of nearshore energy at $t \sim 0.9$, 1.9 correspond to the generation of the first and second outgoing waves whereas the last three are associated with the return to S_s of: (i) the first outgoing wave at $t = 3.3$ and (ii) the second outgoing wave at $t = 5.4$ and 7.7.

In order to investigate the sensitivity of the presented results to the lake and landslide parameters, we study the effect of the lake dimensions (L_a, L_b, α) and slide parameters (s, w, l, v) on the importance of the corner runup, measured as the ratio of maximum corner runup to the average runup on S_s, i.e. $Z_{L_b}/\overline{Z}$ in which $\overline{Z} = (1/L_b)\int_0^{L_b} Z(a = 0,\ b,\ c = 0)\,\mathrm{d}b$. Changes in the parameters and variables are measured relatively to the reference case studied in § 4.2 (i.e. figures 3–7). The

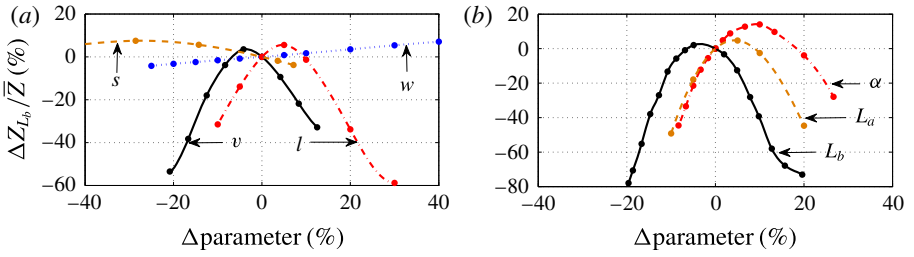

FIGURE 10. (Colour online) Sensitivity of the ratio of the maximum corner runup (normalized by the mean maximum runup) on S_s ($Z_{L_b}/\overline{Z}$) to changes in (*a*) the landslide parameters (s, w, l, v) and (*b*) the lake geometry parameters (L_a, L_b, α). The changes in the parameters are given in per cent and are measured relatively to those used for the reference lake and landslide studied in § 4.2 (i.e. figures 3–7). The other physical and simulation parameters are the same as in figure 3.

relative importance of the corner runup, displayed in figure 10, is clearly very sensitive to the lake geometry (figure 10*b*). For example, a 20 % decrease in the lake width leads to an 80 % drop in the relative corner runup. Figure 10(*b*) therefore further highlights that a change in the lake geometry affects the location and time of positive and negative interference of edge and outgoing waves. The importance of the corner runup is also significantly altered by the length and the velocity of the landslide but is almost independent of the thickness and width of the slide (figure 10*a*). This suggests that uncertainties in the solid landslide length or speed are likely to result in unreliable maximum wave runup predictions.

We would like to finally comment on bottom friction, i.e. on the fact that long waves lose energy due to viscous effects near the seabed (cf. Bernatskiy & Nosov 2012; Geist, Lynett & Chaytor 2009). One way to model bottom friction is to introduce a friction term to the right-hand side of (2.10). A number of different forms of such a dissipation term can be found in the literature that, generally, involve one or more free parameters that can be adjusted for model calibration (e.g. Satake 1995; Synolakis *et al.* 2008; Zelt & Raichlen 1990). For example, the dissipation term suggested by Zelt (1991) reads in two dimensions

$$-\frac{K}{\mu}\frac{\partial(a+X^{(0)},b+Y^{(0)})}{\partial(a,b)}\frac{1}{h_0}\begin{pmatrix}X_t^{(0)}\\Y_t^{(0)}\end{pmatrix}\sqrt{(X_t^{(0)})^2+(Y_t^{(0)})^2}. \tag{4.4}$$

With $K=5\times10^{-5}$ and $\mu\tan\alpha=3/60$, Zelt & Raichlen (1990) showed that their numerical results compared well with the physical experiments of Synolakis (1987) on non-breaking solitary waves running up a 1/20 sloping beach. With the inclusion of this friction term into our model, we obtained less than 2 % maximum runup deviations from the runup values presented in figure 6. This indicates that dissipation by bottom friction can be safely neglected for the results presented here.

5. Conclusions

Under the long-wave and irrotationality assumptions, approximations of Airy type are applied to dynamical equations in Lagrangian coordinates. A numerical scheme based on finite differences is employed to solve the Lagrangian equations and

validated against existing theoretical/numerical results. Aside from the convenience in predicting the motion of the shoreline, which is of significant importance for nonlinear waves, we show that our model can predict reliable post-breaking one-dimensional wave shapes when overturning occurs very close to the shoreline.

For a two-dimensional tsunami in a lake generated by a landslide, the combined influence of edge waves and radiated and reflected waves is examined for a rectangular-shaped basin. It is found that nonlinearities can lead to a significant increase in the maximum inundation compared to that predicted by the linearized equation, and that large runups occur near the lake corners long after the submergence of the slide. The contrast in runup between linear and nonlinear theories is shown to be a result of wave–seabed interactions as well as three-dimensional effects.

The general features and physics reported here apply to the problem of landslide-generated tsunamis in a broad range of lake geometries and shapes. The details, however, may be very different. For instance, in a circular lake, edge waves travel non-stop along the entire perimeter of the lake. This makes the subsequent interactions between edge waves and outgoing waves considerably different. Nevertheless, one would still expect that the combination of outgoing cross-lake waves with edge waves results in extreme inundations. Curved-boundary lakes (e.g. circular or elliptical) may in some cases experience further inundations enhanced by focusing of outgoing waves. Detailed investigation of such scenarios, while beyond the scope of the present manuscript, would be interesting and worth an independent study.

Acknowledgements

We would like to thank A. Zareei and B. S. Howard for careful reading of the manuscript and helpful comments. L.-A.C. was partially funded by the Jaehne Graduate Scholarship and the Frank and Margaret Lucas Scholarship. L.-A.C. and M.-R.A. gratefully acknowledge the support from the American Bureau of Shipping.

REFERENCES

AIRY, G. B. 1841 Tides and waves. In *Encyclopaedia Metropolitana* (ed. H. J. Rose *et al.*), Mixed Sciences, vol. 3, pp. 1817–1845. London.

ATAIE-ASHTIANI, B. & NIK-KHAH, A. 2008 Impulsive waves caused by subaerial landslides. *Environ. Fluid Mech.* **8** (3), 263–280.

BALZANO, A. 1998 Evaluation of methods for numerical simulation of wetting and drying in shallow water flow models. *Coast. Engng* **34**, 83–107.

BERNATSKIY, A. V. & NOSOV, M. A. 2012 The role of bottom friction in models of nonbreaking tsunami wave runup on the shore. *Izv. Atmos. Ocean. Phys.* **48** (4), 427–431.

BRYANT, E. 2008 *Tsunami, The Underrated Hazard*. Springer.

CARRIER, G. F. & GREENSPAN, H. P. 1958 Water waves of finite amplitude on a sloping beach. *J. Fluid Mech.* **4** (1), 97–109.

CARRIER, G. F., WU, T. T. & YEH, H. 2003 Tsunami run-up and draw-down on a plane beach. *J. Fluid Mech.* **475**, 79–99.

DIDENKULOVA, I. & PELINOVSKY, E. 2013 Analytical solutions for tsunami waves generated by submarine landslides in narrow bays and channels. *Pure Appl. Geophys.* **170** (9–10), 1661–1671.

DIDENKULOVA, I., PELINOVSKY, E., SOOMERE, T. & ZAHIBO, N. 2007*a* Runup of nonlinear asymmetric waves on a plane beach. In *Tsunami and Nonlinear Waves* (ed. A. Kundu), pp. 175–190. Springer.

DIDENKULOVA, I. I., KURKIN, A. A. & PELINOVSKY, E. N. 2007*b* Run-up of solitary waves on slopes with different profiles. *Izv. Atmos. Ocean. Phys.* **43** (3), 384–390.

DIDENKULOVA, I. I. & PELINOVSKY, E. N. 2007 Phenomena similar to tsunami in Russian internal basins. *Russian J. Earth Sci.* **8** (6), 1–9.

DI RISIO, M., DE GIROLAMO, P., BELLOTTI, G., PANIZZO, A., ARISTODEMO, F., MOLFETTA, M. G. & PETRILLO, A. F. 2009 Landslide-generated tsunamis runup at the coast of a conical island: new physical model experiments. *J. Geophys. Res.* **114** (C1), 1–16.

DI RISIO, M., DE GIROLAMO, P. & BELTRAMI, G. M. 2011 Forecasting landslide generated tsunamis: a review. In *The Tsunami Threat – Research and Technology* (ed. N.-A. Marner), Forecastin InTech.

FRITS, H. M., MOHAMMED, F. & YOO, J. 2009 Lituya bay landslide impact generated mega-tsunami 50th anniversary. *Pure Appl. Geophys.* **166** (1–2), 153–175.

FRITZ, H. M., HAGER, W. H. & MINOR, H.-E. 2004 Near field characteristics of landslide generated impulse waves. *J. Waterways Port Coast. Ocean Engng* **130** (December), 287–302.

FUJIMA, K. 2007 Tsunami runup in Lagrangian description. In *Tsunami and Nonlinear Waves* (ed. A. Kundu), pp. 191–207. Springer.

GARDNER, J. V., MAYER, L. A. & HUGHS CLARKE, J. E. 2000 Morphology and processes in Lake Tahoe. *Geol. Soc. Amer. Bull.* **112** (5), 736–746.

GEIST, E. L., LYNETT, P. J. & CHAYTOR, J. D. 2009 Hydrodynamic modeling of tsunamis from the Currituck landslide. *Mar. Geol.* **264** (1–2), 41–52.

GENEVOIS, R. & GHIROTTI, M. 2005 The 1963 Vaiont Landslide. *Giorn. Geol. Appl.* 1 **1**, 41–52.

GOTO, C. 1979 Nonlinear equation of long waves in the Lagrangian description. In *Coastal Engineering in Japan,* 22, pp. 1–9.

GOTO, C. & SHUTO, N. 1979 Two-dimensional run-up of tsunami by nonlinear theory. In *Japanese Conference on Coastal Engineering,* 26, pp. 56–60. Japan Society of Civil Engineering. Committee on Coastal Engineering (in Japanese).

GOTO, C. & SHUTO, N. 1980 Run-up of tsunamis by linear and nonlinear theories. *Coast. Engng Proc.* **1** (17), 695–707.

HELLER, V., MOALEMI, M., KINNEAR, R. D. & ADAMS, R. A. 2012 Geometrical effects on landslide-generated tsunamis. *J. Waterways Port Coast. Ocean Engng* **138** (August), 286–298.

JENSEN, A., PEDERSEN, G. K. & WOOD, D. J. 2003 An experimental study of wave run-up at a steep beach. *J. Fluid Mech* **486**, 161–188.

JOHNSGARD, H. & PEDERSEN, G. 1997 A numerical model for three-dimensional runup. *Intl J. Numer. Meth. Fluids* **24** (9), 913–931.

JORSTAD, F. A. 1968 Waves generated by landslides in norwegian fjords and lakes. *Norwegian Geotechnical Institute Publ* 79, pp. 13–32.

KAMPHUIS, J. W. & BOWERING, R. J. 1970 Impulse waves generated by landslides. In *Coastal Engineering Proceedings* **1** (12), 575–588.

KÂNOĞLU, U. 2004 Nonlinear evolution and runup–rundown of long waves over a sloping beach. *J. Fluid Mech.* **513**, 363–372.

LAMB, H. 1932 *Hydrodynamics*. Cambridge University Press.

LIU, P. L.-F., LYNETT, P. & SYNOLAKIS, C. E. 2003 Analytical solutions for forced long waves on a sloping beach. *J. Fluid Mech.* **478**, 101–109.

LIU, P. L.-F., WU, T.-R., RAICHLEN, F., SYNOLAKIS, C. E. & BORRERO, J. C. 2005 Runup and rundown generated by three-dimensional sliding masses. *J. Fluid Mech.* **536**, 107–144.

LOCKRIDGE, P. A. 1990 Nonseismic phenomena in the generation and augmentation of tsunamis. *Nat. Hazards* **3**, 403–412.

LYNETT, P. & LIU, P. L.-F. 2002 A numerical study of submarine-landslide-generated waves and run-up. *Proc. R. Soc. Lond.* A **458** (2028), 2885–2910.

LYNETT, P. & LIU, P. L.-F. 2005 A numerical study of the run-up generated by three-dimensional landslides. *J. Geophys. Res.* **110**, 1–16.

MADSEN, P. A. & SCHÄFFER, H. A. 2010 Analytical solutions for tsunami runup on a plane beach: single waves, N-waves and transient waves. *J. Fluid Mech.* **645**, 27–57.

MEDEIROS, S. C. & HAGEN, S. C. 2013 Review of wetting and drying algorithms for numerical tidal flow models. *Intl J. Numer. Meth. Fluids* **71** (4), 473–487.

MEI, C. C., STIASSNIE, M. & YUE, D. K.-P. 2005 Refraction by slowly varying depth. In *Theory and Applications of Ocean Surface Waves – Part 1*, Advanced edn, chap. 3, pp. 65–121. World Scientific.

MEYER, R. E. 1986*a* On the shore singularity of water waves. I. The local model. *Phys. Fluids* **29** (10), 3152–3163.

MEYER, R. E. 1986*b* On the shore singularity of waterwave theory. II. Small waves do not break on gentle beaches. *Phys. Fluids* **29** (10), 3164–3171.

MICHE, A. 1944 Mouvements ondulatoires de la mer en profondeur croissante ou décroissante. *Ann. des Ponts et Chaussees* **114** (1), 131–164.

PANIZZO, A., DE GIROLAMO, P. & PETACCIA, A. 2005*a* Forecasting impulse waves generated by subaerial landslides. *J. Geophys. Res.* **110** (C12), C12025.

PANIZZO, A., DE GIROLAMO, P., DI RISIO, M., MAISTRI, A. & PETACCIA, A. 2005*b* Great landslide events in Italian artificial reservoirs. *Nat. Hazards Earth Syst. Sci.* **5**, 733–740.

PEDERSEN, G. & GJEVIK, B. 1983 Run-up of solitary waves. *J. Fluid Mech.* **135**, 283–299.

PELINOVSKY, E. N. & MAZOVA, R. KH. 1992 Exact analytical solutions of nonlinear problems of tsunami wave run-up on slopes with different profiles. *Nat. Hazards* **6**, 227–249.

RYBKIN, A., PELINOVSKY, E. & DIDENKULOVA, I. 2014 Nonlinear wave run-up in bays of arbitrary cross-section: generalization of the Carrier–Greenspan approach. *J. Fluid Mech.* **748**, 416–432.

SAMMARCO, P. & RENZI, E. 2008 Landslide tsunamis propagating along a plane beach. *J. Fluid Mech.* **598**, 107–119.

SATAKE, K. 1995 Linear and nonlinear computations of the 1992 Nicaragua earthquake tsunami. In *Tsunamis: 1992–1994*, vol. 144, pp. 455–470. Birkhäuser.

SHUTO, N. 1967 Run-up of long waves on a sloping beach. *Coastal Engineering in Japan* **10**, 23–38.

SHUTO, N. 1968 Three-dimensional behaviour of long waves on a sloping beach. *Coastal Engineering in Japan, JSCE* **11**, 53–57.

SHUTO, N. 1972 Standing waves in front of a sloping dike. In *Coastal Engineering Proceedings* **1** (13), pp. 1629–1647.

SHUTO, N. & GOTO, C. 1978 Numerical simulation of tsunami run-up. *Coast. Engng Japan* **21**, 13–20.

SPIELVOGEL, L. Q. 1975 Single-wave run-up on sloping beaches. *J. Fluid Mech.* **74** (4), 685–694.

SYNOLAKIS, C. E. 1987 The runup of solitary waves. *J. Fluid Mech.* **185**, 523–545.

SYNOLAKIS, C. E., BERNARD, E. N., TITOV, V. V., KÂNOĞLU, U. & GONZÁLEZ, F. I. 2008 Validation and verification of tsunami numerical models. *Pure Appl. Geophys.* **165** (11–12), 2197–2228.

TADEPALLI, S. & SYNOLAKIS, C. E. 1994 The run-up of N-waves on sloping beaches. *Proc. R. Soc. Lond.* A **445** (1923), 99–112.

TCHAMEN, G. W. & KAHAWITA, R. A. 1998 Modelling wetting and drying effects over complex topography. *Hydrol. Process.* **1182** (February), 1151–1182.

TUCK, E. O. & HWANG, L. S. 1972 Long wave generation on a sloping beach. *J. Fluid Mech.* **51** (3), 449–461.

VOIGHT, B., JANDA, R. J., GLICKEN, H. & DOUGLASS, P. M. 1983 Nature and mechanics of the Mount St Helens Rockslide-avalanche of 18 May 1980. *Geotechnique* **33**, 243–273.

WALDER, J. S., WATTS, P., SORENSEN, O. E. & JANSSEN, K. 2003 Tsunamis generated by subaerial mass flows. *J. Geophys. Res.* **108** (B5), 2236, 19 pages (noted as 2–1 to 2–19 on article).

WEISS, R., FRITZ, H. M. & WÜNNEMANN, K. 2009 Hybrid modeling of the mega-tsunami runup in Lituya Bay after half a century. *Geophys. Res. Lett.* **36** (9), L09602.

YEH, H. H., LIU, P. L.-F. & SYNOLAKIS, C. E. 1996 *Long-wave Runup Models: Friday Harbor, USA, 12–17 September 1995*. World Scientific.

ZABUSKY, N. J. 1962 Exact solution for the vibrations of a nonlinear continuous model string. *J. Math. Phys.* **3** (5), 1028–1039.

ZAHIBO, N., PELINOVSKY, E. N., GOLINKO, V. & OSIPENKO, N. 2006 Tsunami wave runup on coasts of narrow bays. *Intl J. Fluid Mech. Res.* **33**, 1–18.

ZELT, J. A. 1986 Tsunamis, the response of harbours with sloping boundaries to long wave excitation, PhD thesis, California Institute of Technology.

ZELT, J. A. & RAICHLEN, F. 1990 A Lagrangian model for wave-induced harbour oscillations. *J. Fluid Mech.* **213**, 203–225.

ZELT, J. A. 1991 The run-up of nonbreaking and breaking solitary waves. *Coast. Engng* **15** (3), 205–246.